

# Calibration and Image Reconstruction Techniques for FMCW MIMO Radars with Consideration of Antenna Radiation Patterns

Kalibrations- und Bildrekonstruktionsverfahren für  
FMCW-MIMO-Radare unter Berücksichtigung der  
Antennenabstrahlungscharakteristik

Daniel Gotzens

Masterarbeit vorgelegt dem



Institut für  
Hochfrequenz-  
technik



Lehrstuhl für Radarsystemtechnik  
Institut für Hochfrequenztechnik  
RWTH Aachen University  
February 15, 2024

In Kooperation mit



indurad GmbH Aachen

### **Abstract**

Increased image quality can be achieved by implementing backprojection on a millimeter-wave TDM FMCW MIMO Radar. In this thesis, a backprojection-based imaging algorithm is proposed and implemented for a radar sensor. This radar sensor's functionality is tested, the sensor is calibrated, and then the algorithm is compared to the current FFT-based algorithm as well as MUSIC. It is found that near-field accuracy of the image generated with backprojection and MUSIC is increased, and that real-time capability can only be guaranteed for backprojection and the current FFT-based approach.

# Contents

<b>1</b>	<b>Introduction</b>	<b>2</b>
1.1	Theoretical Background . . . . .	5
1.1.1	Signal Model . . . . .	5
1.1.2	Calibration . . . . .	7
1.1.3	Image Reconstruction . . . . .	7
1.2	Physical Setup . . . . .	11
<b>2</b>	<b>Calibration</b>	<b>13</b>
2.1	Stability Analysis . . . . .	13
2.1.1	Setup . . . . .	14
2.1.2	Results . . . . .	16
2.2	Calibration . . . . .	19
2.2.1	Setup . . . . .	19
2.2.2	Results . . . . .	21
<b>3</b>	<b>Image Reconstruction</b>	<b>30</b>
3.1	Implementation . . . . .	30
3.2	Results . . . . .	30

# Chapter 1

## Introduction

Radar technology has undergone significant advancements over the decades, revolutionizing various fields including aerospace, defense, automotive, and healthcare. Its fundamental principle of using electromagnetic waves to detect the presence, direction, distance, and speed of objects has enabled myriad applications, ranging from weather monitoring to target tracking.

Within this expansive domain, Frequency Modulated Continuous Wave (FMCW) Multiple Input Multiple Output (MIMO) Millimeter Wave (mmWave) radar systems have emerged as a cutting-edge solution with unparalleled capabilities. FMCW radar, characterized by its continuous transmission of frequency-modulated signals, combined with MIMO architecture, which utilizes multiple antennas for both transmission and reception, has enabled enhanced spatial resolution, improved target detection, and increased resilience to interference. Operating in the mmWave spectrum, typically within the frequency range of 24 to 100 GHz, these radars offer advantages such as high resolution, immunity to environmental conditions like fog and precipitation, and the ability to accommodate large bandwidths for high data rates.

The fusion of FMCW, MIMO, and mmWave technologies represents a significant leap forward in radar sensing, promising to address the evolving demands of modern applications ranging from autonomous vehicles to biomedical imaging. This thesis endeavors to contribute to this dynamic field by proposing and evaluating novel imaging algorithms optimized for FMCW MIMO mmWave radar systems, with a focus on enhancing their performance, efficiency, and applicability across diverse scenarios and applications.

Radar technology finds diverse applications across various industries, with one notable area being mining. In the mining sector, radar systems play a crucial role in enhancing safety, efficiency, and productivity.

Radar-based collision avoidance systems are employed in mining operations to prevent accidents involving heavy machinery and personnel. These systems utilize radar sensors to detect nearby objects and provide real-time alerts to operators, facilitating safe maneuvering in challenging environments.

Moreover, radar technology is instrumental in various logistical aspects of mining operations. It is utilized for stockpile management, enabling accurate measurement and monitoring of ore and waste material reserves, optimizing inventory control and resource allocation. Radar sensors are also integrated into silo and train loading processes, ensuring efficient and precise transfer of bulk materials onto transport vehicles. Furthermore, radar-based systems facilitate ship unloading and berthing operations at port facilities, streamlining the handling of bulk commodities. One significant advantage of radar systems over visual-based solutions in mining environments is their resilience to omnipresent dust and grime. Unlike optical systems, radar sensors are not affected by adverse weather conditions or obstructed visibility, ensuring reliable performance and continuous operation even in harsh mining environments.

In the realm of radar sensing, various approaches exist for achieving multidimensionality in imaging. Traditional radar systems employ one-dimensional (1D) sensors, which provide information along a single axis, typically range. These sensors are adept at measuring distances to targets but lack detailed spatial information. To overcome this limitation, two-dimensional (2D) sensors have been developed, capable of scanning in both range and azimuth dimensions, providing a more comprehensive view of the surrounding environment. These sensors often achieve multidimensionality either mechanically, by utilizing mechanisms such as rotating antennas or electronically with phased arrays to sweep the radar beam across the scene. Additionally, three-dimensional (3D) radar sensors offer even greater spatial resolution by adding an elevation dimension to the azimuth and range measurements. These sensors are commonly used in applications requiring detailed volumetric imaging. The mechanical movement or rotation of the sensor enables it to scan the scene from multiple angles, capturing information in three dimensions.

The evolution of radar technology has led to the development of advanced imaging techniques that leverage the principles of Multiple Input Multiple Output (MIMO) radar systems. These systems, characterized by their use of multiple transmit and receive antennas, offer significant improvements in imaging performance compared to traditional radar architectures. One key advantage of MIMO radar is its ability to achieve multidimensional imaging without the need for mechanically rotating antennas. By utilizing multiple antennas in a static configuration, MIMO radar systems can capture spatial information along multiple dimensions simultaneously, leading to enhanced imaging capabilities at reduced cost and complexity. Additionally, MIMO radar systems offer the potential for higher frame rates compared to traditional radar systems. With multiple antennas operating in parallel, MIMO radar can sample the scene more frequently, enabling rapid data acquisition and real-time imaging of dynamic environments. The next step in the advancement of MIMO imaging radars involves the development and optimization of sophisticated signal processing algorithms tailored to exploit the full potential of these systems. These algorithms aim to extract rich spatial information from the received signals, enabling

high-fidelity imaging of complex scenes with unprecedented detail and accuracy.

Current 3D imaging algorithms employed for many FMCW MIMO radars rely on the Fast Fourier Transform (FFT) technique for generating three-dimensional reconstructions of the observed scene. This algorithm computes each dimension of the image by performing an FFT on a different dimension of the Intermediate Frequency (IF) signal obtained from the radar’s input data.

Specifically, the range dimension corresponds to the time dimension of the input signal, while the azimuth and elevation dimensions are computed from horizontal and vertical channels, respectively. One of the primary strengths of this approach lies in its fast implementation, allowing for rapid processing of radar data. However, despite its efficiency, the FFT-based algorithm suffers from several limitations.

These include near-field distortion issues, restrictions in applicability to Uniform Linear Arrays (ULA), the necessity for array calibration, and the inability to utilize measured antenna gains effectively. Moreover, the algorithm is prone to ringing artifacts, which can degrade the quality of reconstructed images, particularly in complex or cluttered environments.

In response to the limitations of the current FFT-based approach, a novel back projection algorithm is proposed for 3D imaging in the FMCW MIMO radar system. Unlike the FFT-based method, the proposed algorithm offers increased flexibility and versatility in image reconstruction. One of its key advantages is the elimination of ringing artifacts, which commonly plague FFT-based reconstructions. Additionally, the back projection algorithm is capable of addressing near-field distortion issues and is suitable for both near- and far-field imaging scenarios. Moreover, it exhibits compatibility with non-ULA arrays, enabling broader applicability across different radar configurations. A notable feature of the proposed algorithm is its ability to incorporate measured antenna gains effectively, leading to more accurate and reliable imaging results. By leveraging these advantages, the back projection algorithm promises to significantly enhance the imaging capabilities of the FMCW MIMO radar, paving the way for improved performance and expanded applications in various domains.

In this thesis, we embark on a comprehensive exploration of advanced imaging techniques for FMCW MIMO radar systems, aiming to address existing challenges and enhance imaging performance.

Chapter 1 provides a thorough examination of the theoretical background underpinning radar imaging, including signal models and a detailed description of the image reconstruction methods. We delve into the intricacies of both FFT-based and proposed back projection algorithms. Furthermore, a detailed hardware description of the FMCW MIMO radar system under investigation is presented, laying the foundation for subsequent experimental chapters.

Chapter 2 focuses on measurements and validation of hardware stability through extensive static measurements. Through rigorous analysis, we assess the stability of the radar system and measure antenna gains, crucial for accurate

imaging.

Chapter 3 shifts the focus to imaging algorithms, detailing the implementation of the back projection algorithm using PyTorch. Additionally, we discuss the interpolation of measured gains and evaluate the performance enhancements achieved through these refinements.

By presenting comprehensive results and analyses, this thesis aims to contribute to the advancement of FMCW MIMO radar imaging technology, with implications for various applications in fields such as remote sensing, autonomous vehicles, and surveillance.

## 1.1 Theoretical Background

This section provides a foundation for understanding the principles and methodologies underpinning FMCW MIMO radar imaging. We begin by elucidating the signal model employed in FMCW radar systems, elucidating the distinctions between single-channel and MIMO configurations. Subsequently, we delve into the intricacies of image reconstruction techniques, exploring both the Discrete Fourier Transform (DFT) approach and the proposed backprojection algorithm.

### 1.1.1 Signal Model

Understanding the signal model is fundamental to grasp the operation and capabilities of FMCW MIMO radar systems. In this section, we delve into the intricacies of the signal model, beginning with an exploration of Single Channel Frequency Modulated Continuous Wave (FMCW) radar systems. We clarify the key principles governing their signal generation and processing, laying the groundwork for a comprehensive understanding of radar imaging techniques. Then, we extend our analysis to encompass Multiple Input Multiple Output (MIMO) FMCW radar systems, highlighting the unique characteristics and complexities associated with their signal model.

#### Single Channel FMCW

A single channel consists of a transmit antenna and a receive antenna. The transmit antenna sends a so-called chirp of duration  $T_{chirp}$ , which is a sinusoid with linearly increasing frequency. The signal  $x_{TX}(t)$  sent by the transmit antenna is reflected by an ideal point scatterer at position  $\vec{r}_S$  and then received at the receive antenna as  $x_{RX}(t)$ . The propagation delay  $\tau$  can be calculated using the speed of light  $c_0$ , and the locations of the receive and transmit antennas  $\vec{r}_{RX}$  and  $\vec{r}_{TX}$ :

$$\tau = \frac{\|\vec{r}_{TX} - \vec{r}_S\| + \|\vec{r}_{RX} - \vec{r}_S\|}{c_0} \quad (1.1)$$

Using a complex representation for the in-phase and quadrature components of the signal, the transmit and receive signal can be formulated for  $t \in [0, T_{chirp}]$ :

$$x_{TX}(t) = A_0 e^{j(\omega_0 t + \frac{1}{2} \dot{\omega} t^2 + \phi_0)} \quad (1.2)$$

$$x_{RX}(t) = A(\vec{r}_S) x_{TX}(t - \tau) \quad (1.3)$$

$$(1.4)$$

The received signal is then mixed with a copy of the transmitted signal (1.2) and a low-pass filter is applied. The resulting signal  $y(t)$  is called *intermittent frequency* signal.

$$y(t) = \text{LP} \{x_{RX}(t) \cdot x_{TX}(t)\} \quad (1.5)$$

$$= \text{LP} \left\{ A_0 e^{j(\omega_0 t + \frac{1}{2} \dot{\omega} t^2)} \cdot A(\vec{r}_S) A_0 e^{j(\omega_0(t - \tau(\vec{r})) + \frac{1}{2} \dot{\omega}(t - \tau(\vec{r}))^2)} \right\} \quad (1.6)$$

$$= A_0^2 A(\vec{r}_S) e^{j(\frac{1}{2} \dot{\omega} \tau^2(\vec{r}_S) - \omega_0 \tau)} \cdot \text{LP} \left\{ e^{j(2\omega_0 t + \frac{1}{2} \dot{\omega} t^2 - \dot{\omega} \tau t)} \right\} \quad (1.7)$$

$$\approx G(\vec{r}_S) e^{-j\dot{\omega} \tau t} \quad (1.8)$$

The fact that the IF-signal contains all the information – i.e. the IF signal's frequency directly corresponds to the target's distance – explains the main advantage of this technology. The carrier frequency can be orders of magnitude higher than the intermittent frequency, which drastically reduces the requirements for the subsequent signal processing, while retaining the improved resolution due to the smaller wavelengths of the carrier frequency.

FIND QUOTE: "GHz resolution for MHz processing"

To locate a target in the cross-range dimensions, a single-channel FMCW-radar can be used to scan in multiple directions, by either rotating the antennas, redirecting their beam with rotating mirrors, or with beamforming antenna arrays. In any case, this requires highly directive antennas and also increases size, weight and cost of a radar sensor.

## MIMO FMCW

Multiple-input multiple-output radar benefits from increased diversity and signal power. If  $N_{TX}$  transmit antennas and  $N_{RX}$  receive antennas are employed,  $K = N_{TX} \cdot N_{RX}$  channels are available. To differentiate the signals from each other, a multiplexing technique has to be chosen. Options include time division multiplex, frequency division multiplex and code division multiplex.

In TDM, multiple access is achieved by the transmit antennas all send one after another, while all receive antennas receive simultaneously. In FDM, simultaneous transmission is made possible by subdividing the bandwidth and assigning a different frequency range to each antenna. That means that TDM allows for higher bandwidths for each transmission, while FDM allows higher transmission durations.



In CDM, both simultaneous transmission and use of the entire bandwidth is made possible by using a different waveform to each channel. However, processing at the carrier frequency is required to differentiate the signals from another, as opposed to TDM and FMD, where all processing can be done at the intermittent frequency range.

Depending on the application, a compromise has to be found between the advantages and drawbacks of each method. There are also methods available that combine aspects of these three basic paradigms, such as OFDM and Hadamard-Coding.[citation needed]

Once the received signals are demultiplexed, the ideal receive signal for antenna pair  $k \in \{0, 1, \dots, K-1\}$ :

$$y_k(t) = G_k(\vec{r}_S) e^{-j\dot{\omega}\tau_k(\vec{r}_S)t} \quad (1.9)$$

Note that both the gain and the propagation delay may differ from channel to channel.

In reality, the scene can consist of multiple and expansive scatterers, that reflect the transmitted signals at different intensities. which is summarized as a locational reflectivity  $F_k(\vec{r})$ .<sup>1</sup> Also, interference and electric noise may be present in each channel, which we summarize as  $n_k(t)$ . Thus, the overall IF-signal is:

$$y_k(t) = \iiint F_k(\vec{r}) G_k(\vec{r}) e^{-j\dot{\omega}\tau_k(\vec{r})t} d\vec{r} + n_k(t) \quad (1.10)$$

$$(1.11)$$

After sampling the signal at sampling intervals  $T_s$  such the sampling frequency  $f_s = \frac{1}{T_s}$  is sufficiently high:  $2f_s > \frac{1}{2\pi}(\omega_0 + \dot{\omega}T_{chirp})$ , and with  $M$  samples such that  $MT_s < T_{chirp}$ , the sampled IF-signal can be defined as:

$$y_k[m] = y_k(t = mT_s), \text{ for } m \in \{0, 1, \dots, M-1\} \quad (1.12)$$

### 1.1.2 Calibration

### 1.1.3 Image Reconstruction

Image reconstruction is an inverse problem where the locational reflectivity of the scene  $F(\vec{r})$  has to be estimated from the received signals  $y_k[m]$ . Multiple approaches are available; in the following, three will be presented.

---

<sup>1</sup>The index  $k$  is introduced here to take obstructed visibility into account: from the point of view of one channel, two scatterers may be visible simultaneously, while from the point of view of another, one might obstruct the other's visibility.

## Discrete Fourier Transform

The discrete fourier transform can be implemented with high efficiency, and many CPUs even include silicone-based implementations [citation needed]. In this approach, the DFT is applied over three dimensions of the input signal, obtaining a discrete output signal in spherical coordinates whose amplitude is an estimate of the locational reflectivity.

For each input channel, the range of a target can be estimated by applying the DFT over time. The resulting spectrum's peak corresponds to the target:

$$\mathcal{F}_m\{y_k[m]\}(\Omega) = \sum_{m=0}^{M-1} e^{-j2\pi \frac{m\Omega}{M}} y_k[m] \quad (1.13)$$

$$= G_k(\vec{r}_S) \delta(\Omega - \dot{\omega} \tau_k(\vec{r}_S) T_s) \quad (1.14)$$

In order to understand how information on the direction of a target can be extracted from the channel data, we consider an ideal  $1 \times K$  horizontal uniform linear array (*ULA*) where the spacing is exactly  $d = \frac{\lambda_0}{2}$ , with  $\lambda_0 = \frac{c_0}{f_0}$ . The antennas are located at  $\vec{r}_{TX} = \vec{0}$  and  $\vec{r}_{RX,k} = (kd, 0, 0)^T$ . A scatterer located at  $\vec{r}_S = (r_S \sin \theta_S, r_S \cos \theta_S, 0)^T$  reflects the transmitted radar waves with an intensity of  $A_S$ . Then, their runtime across the array is:

$$\tau_k = \frac{1}{c_0} (\|\vec{r}_{TX} - \vec{r}_S\| + \|\vec{r}_{RX} - \vec{r}_S\|) \quad (1.15)$$

$$(1.16)$$

In far-field conditions, the target is far enough ( $r \gg Kd$ ) away for the reflected wavefronts to be planar. That means that the runtime can then be approximated as such:

$$\tau_k \approx 2r_S + kd \sin \theta_S \quad (1.17)$$

In equation 1.7 it can be seen that the locational gain  $G(\vec{r})$  contains a phase shift depending on the runtime of the waves:

$$G_k(\vec{r}) = A_S A_k(\vec{r}) e^{j(\frac{1}{2} \dot{\omega} \tau_k^2 - \omega_0 \tau_k)} \quad (1.18)$$

$$\approx A_S A_k(\vec{r}) e^{-j\omega_0 \tau_k} \quad (1.19)$$

Assuming the attenuation along the path is channel-independent, the signals

can all be considered copies of each other:

$$y_k(t) = A_S A_k(\vec{r}) e^{-j\omega_0 \tau_k} e^{-j\dot{\omega} \tau_k t} \quad (1.20)$$

$$= A_S A_k(\vec{r}) e^{-j\frac{\omega_0}{c_0}(2r_S + kd \sin \theta_S)} e^{-j\frac{\dot{\omega}}{c_0}(2r_S + \overbrace{kd \sin \theta_S}^{\ll 2r_S})t} \quad (1.21)$$

$$= A_S A_0(\vec{r}) e^{-j\frac{\omega_0}{c_0}2r_S} e^{-j\frac{\dot{\omega}}{c_0}2r_S t} e^{-j\frac{\omega_0}{c_0}kd \sin \theta_S} \quad (1.22)$$

$$= y_0(t) e^{-j\frac{\omega_0}{c_0}kd \sin \theta_S} \quad (1.23)$$

$$\Rightarrow y_k[m] = y_k(t = mT_S) = y_0[m] e^{-j\frac{\omega_0}{c_0}kd \sin \theta_S} \quad (1.24)$$

Applying the DFT accross the ULA yields:

$$\mathcal{F}_k\{y_k[m]\}(\Omega) = \mathcal{F}_k\{y_0[m] e^{-j\frac{\omega_0}{c_0}kd \sin \theta_S}\}(\Omega) \quad (1.25)$$

$$= y_0[m] \cdot \delta\left(\Omega - \frac{\omega_0}{c_0}(d \sin \theta_S)\right) \quad (1.26)$$

$$= y_0[m] \cdot \delta(\Omega - \pi \sin \theta_S) \quad (1.27)$$

$$(1.28)$$

The azimuth angle  $\theta_S$  can be extracted from the signal supplied by a horizontal ULA. Analogously, the elevation angle  $\phi_S$  can be obtained with a vertical ULA. If a  $1 \times K$  array is used, where the  $K$  receive antennas form a uniformly spaced grid, successive DFTs across the rows and columns of this grid yield two dimensions. However, the same can be achieved with fewer antennas in a MIMO configuration.

The *virtual array* of a MIMO array is a corresponding SIMO array. It has the same number of channels: if the original array is  $N_{TX} \times N_{RX}$ , the virtual array has  $1 \times K$  channels, where  $K = N_{TX} \cdot N_{RX}$ .

The virtual transmit and receive antenna associated with channel  $k = 0$  are placed in the origin of the virtual array's coordinate system. The other receive antennas are then placed such that the displacement between them and the transmit antenna is the same as it was between the original MIMO array's corresponds transmit and receive antenna. It is possible for virtual antennas to be at the same location.

Overall, a 3D image in range, azimuth, and elevation is generated by calculating the DFT over time, and the DFTs over the rows and columns of the virtual array. For this to work, the scatterer needs to be distant enough for the wavefronts to be planar, and the virtual array's grid needs to be uniformly spaced with  $d = \lambda_0/2$  spacing.

## Backprojection

Compared to the DFT-based approach, backprojection takes fewer approximations and requirements on the array to work, while using a similar amount of

computation. The approach works by correlating the input signal  $y_k[m]$  to the theoretical signal  $s_k[m, \vec{r}]$  of an ideal scatterer at different locations. The mean correlation of all channels to the theoretical signal is then used as an estimate for the locational reflectivity:

$$\hat{F}(\vec{r}) = \frac{1}{K} \sum_{k=0}^{K-1} s_k[m, \vec{r}] \star y_k[m] \quad (1.29)$$

$$= \frac{1}{K} \sum_{k=0}^{K-1} \sum_{m=0}^M s_k^*[m, \vec{r}] y_k[m] \quad (1.30)$$

Using the signal model from (1.9) yields:

$$\hat{F}(\vec{r}) = \frac{1}{K} \sum_{k=0}^{K-1} \sum_{m=0}^M G_k^*(\vec{r}) e^{+j\dot{\omega}\tau_k(\vec{r}_S)mT_s} y_k[m] \quad (1.31)$$

To reduce the computational intensity of this algorithm, calculating the inner sum (over  $m$ ) can be rewritten as an inverse discrete fourier transform (IDFT):

$$\hat{F}(\vec{r}) = \frac{1}{K} \sum_{k=0}^{K-1} G_k^*(\vec{r}) \sum_{m=0}^M e^{+j\dot{\omega}\tau_k(\vec{r}_S)mT_s} y_k[m] \quad (1.32)$$

$$= \frac{1}{K} \sum_{k=0}^{K-1} G_k^*(\vec{r}) \sum_{m=0}^M e^{j\Omega m} y_k[m] \Big|_{\Omega=\dot{\omega}\tau_k(\vec{r}_S)T_s} \quad (1.33)$$

$$= \frac{1}{K} \sum_{k=0}^{K-1} G_k^*(\vec{r}) \mathcal{F}_m^{-1} \{y_k[m]\} (\Omega = \dot{\omega}\tau_k(\vec{r}_S)T_s) \quad (1.34)$$

## MUSIC

The Multiple Signal Classification (MUSIC) algorithm can also be used to estimate the locational reflectivity of a scene. It operates on the time-domain fourier transform of the IF-signal, and makes similar far-field approximations as the DFT-based approach. The abstract signal model for MUSIC is:

$$\mathbf{y}(t) = \mathbf{A} \cdot \mathbf{s}(t) + \mathbf{n}(t) \quad (1.35)$$

Here,  $\mathbf{y}, \mathbf{n} \in \mathbb{C}^K$ ,  $\mathbf{A} \in \mathbb{C}^{K \times Z}$ , and  $\mathbf{s} \in \mathbb{C}^Z$ .  $Z$  is the number of voxels in the output image and  $K$  the number of receive channels. For example, if the output image consist of  $X \times Y \times Z$  cuboid voxels, then  $Z = X \cdot Y \cdot Z$ .

Thus, the support matrix  $\mathbf{A}$  is a linear transform from the locational reflectivity  $\mathbf{s}$  to the expected input signal vector  $\mathbf{y}$ . Each column vector  $\mathbf{a}_z$  of the support matrix  $\mathbf{A}$  therefor corresponds to the expected input signal vector caused by a point source.

The MUSIC algorithm revolves around the correlation matrix of its input signal  $\mathbf{R}_{\mathbf{y}\mathbf{y}}$ . Assuming the a stationary scene with zero-mean noise of covariance  $\mathbf{C}_{\mathbf{nn}}$ , it follows that

$$\mathbf{R}_{\mathbf{y}\mathbf{y}} = \mathbb{E}\{\mathbf{y}\mathbf{y}^H\} \quad (1.36)$$

$$= \mathbf{A}\mathbf{R}_{\mathbf{ss}}\mathbf{A}^H + \mathbf{C}_{\mathbf{nn}}, \text{ with } \mathbf{R}_{\mathbf{ss}} := \mathbb{E}\{\mathbf{s}\mathbf{s}^H\} \quad (1.37)$$

Assume that  $\mathbf{R}_{\mathbf{ss}}$  is nonsingular with rank  $q$  and that  $\mathbf{A}$  has full rank. If  $\mathbf{R}_{\mathbf{y}\mathbf{y}}$  has  $p$  eigenvalues, then the smallest  $p - q$  of them are all  $\sigma^2$ , and their corresponding eigenvectors – i.e. the columns of  $\mathbf{C}_{\mathbf{nn}}$  – are all orthogonal to the support vectors  $\mathbf{a}_z$ .

This property is key to the MUSIC algorithm. The metric used to generate an image is the projection of  $\mathbf{a}_z$  onto the  $\mathbf{C}_{\mathbf{nn}}$ . Due to their orthogonality, the projection of support vectors corresponding to a signal source will be zero. The image intensity at voxel  $z$  is thus defined computed as the normalized inverse square magnitude of this projection:

$$P_{MUSIC}[z] = \frac{\mathbf{a}_z^H \mathbf{a}_z}{\mathbf{a}_z^H \hat{\mathbf{C}}_{nn}^H \hat{\mathbf{C}}_{nn} \mathbf{a}_z} \quad (1.38)$$

The input signals are often highly correlated, due to phenomena such as multipath propagation or inter-channel crosstalk. This unfortunately means that nonsingularity of  $\mathbf{R}_{\mathbf{ss}}$  cannot always be guaranteed. A preprocessing step is required to “decorrelate” the signals and thereby making  $\mathbf{R}_{\mathbf{ss}}$  singular again.

While early schemes, such as the “3/4in plywood” spacial dither algorithm by Widrow *et al.* [CITE] consisted of mechanically moving the receive antenna array orthogonal to the look direction, preprocessing can also be done after receiving the signal.

Spacial smoothing, as proposed by [CITE], improves the correlation matrix’s eigenstructure by

## 1.2 Physical Setup

The sensor employed in this thesis operates on Multiple Input Multiple Output (MIMO) Frequency Modulated Continuous Wave (FMCW) technology, showcasing advanced features tailored for precise radar imaging. It offers a range capability of less than 100 meters, extendable up to 800 meters with active beamforming techniques. The sensor achieves a remarkable range resolution of 3.8 millimeters, enabling detailed imaging of objects within its detection range.

Utilizing a sawtooth or chirp signal type, the sensor employs Time Division Multiplexing (TDM) in Transmission (Tx) for efficient multiplexing. Operating within the frequency range of 77 to 81 gigahertz (GHz), it leverages the millimeter-wave spectrum to achieve high-resolution imaging suitable for a variety of applications.

The chirp duration of the sensor is between 60 to 70 microseconds, ensuring effective signal processing and data acquisition. Equipped with 12 transmit (Tx) antennas and 16 receive (Rx) antennas, the sensor offers comprehensive coverage and sensitivity, facilitating robust imaging performance.

Furthermore, the sensor's Intermediate Frequency (IF) samplerate is set at 22 megahertz (MHz), providing sufficient bandwidth for accurate signal processing and analysis. This combination of advanced features and specifications positions the sensor as a versatile and effective tool for radar imaging tasks in diverse scenarios, ranging from automotive safety systems to industrial sensing applications.

# Chapter 2

## Calibration

In order to achieve high fidelity imaging, any systematic offsets of the radar sensor must be compensated. In this chapter, the systematic errors of the radar are observed and classified. With knowledge of their stability and overall characteristics, the array's antenna gains are measured and the array is calibrated with these results.

The first part of this chapter (sec. 2.1) focuses on stability analysis, which is conducted through long-term static measurements of a corner reflector. By monitoring the radar system's performance over an extended period, we aim to assess its stability and reliability in real-world operating conditions. The analysis provides insights into any temporal variations or drifts in system parameters, enabling proactive measures to mitigate potential sources of error.

The second part of this chapter (sec. 2.2) focuses on antenna gain measurements using a rotating setup. Antenna gain plays a crucial role in radar imaging, affecting the system's sensitivity and resolution. By rotating the radar system and precisely measuring the received signals from known targets, we can accurately determine the antenna gain across different azimuth angles. This measurement process enables the characterization and validation of antenna performance, facilitating improved imaging accuracy and consistency.

Through these procedures, Chapter 2 aims to establish a robust foundation for the subsequent imaging algorithms that are implemented and evaluated in Chapter 3. By ensuring the stability of system parameters and accurately characterizing antenna performance, we strive to enhance the reliability and effectiveness of FMCW MIMO radar imaging for various applications.

### 2.1 Stability Analysis

In this section, we delve into evaluating the stability of the radar system through a comprehensive analysis of its response under static conditions. By observing the system's behavior over an extended period, our objective is to identify and

characterize any temporal variations or drifts in system parameters. This assessment is crucial for understanding the inherent stability of the radar system and for identifying potential sources of instability that may impact imaging performance. Through rigorous stability analysis, we aim to enhance the accuracy, consistency, and reliability of radar imaging results, laying a solid foundation for subsequent experiments and applications.

In our stability analysis, we meticulously investigate several key parameters to assess their impact on radar system performance and calibration. These parameters include system restart, time elapsed since system restart, system temperature, and the frequency of the deramped signal. Each of these parameters plays a crucial role in determining the stability and reliability of radar imaging, making them essential targets for investigation during calibration procedures.

Firstly, we examine the influence of time elapsed since system restart on radar stability. Over time, certain components of the radar system may undergo gradual changes or drifts, affecting signal quality and imaging precision. By monitoring the system's response over varying time intervals, we can assess the magnitude and nature of these temporal variations and devise strategies to mitigate their impact on calibration.

Secondly, we scrutinize the effects of system restarts on radar performance. System restarts can introduce transient variations in system behavior, potentially leading to fluctuations in signal characteristics and imaging accuracy. Understanding how the radar system responds to restart events is critical for ensuring consistent performance and minimizing calibration errors.

Furthermore, we investigate the dependence of radar system performance on system temperature. Temperature fluctuations can influence the characteristics of electronic components, potentially introducing biases and inaccuracies in radar measurements. By quantifying the effects of temperature variations on radar stability, we can implement temperature compensation techniques to enhance calibration accuracy and reliability.

### 2.1.1 Setup

The sensor is placed in a low-reflection environment and a corner reflector is placed at boresight in front of the sensor at a distance of roughly 1.60 m (cf. 2.1). The time data collected in all channels is recorded every minute. The temperature readings of the sensor's CPU, FPGA and radar frontend are also recorded every minute (cf. 2.2). The experiment is repeated with a different ramp slope  $\dot{\omega}$  in order to achieve a different frequency of the deramped signal, since

$$f_{IF} = \dot{\omega} \cdot \frac{2r_{refl}}{c} \quad (2.1)$$

Due to the geometry of the setup, the runtime of each transmitted wavefront should be identical. Thus, the ideal deramped signal should be of a single, constant frequency and without inter-channel phase differences. In practice, the



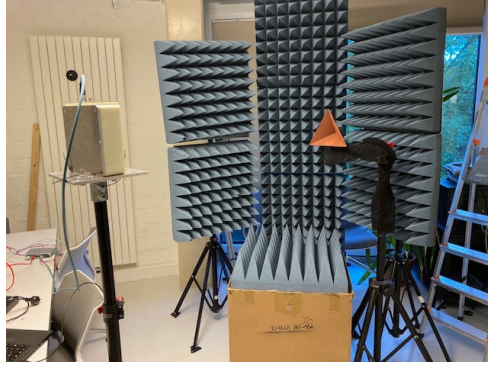


Figure 2.1: Measurement Setup

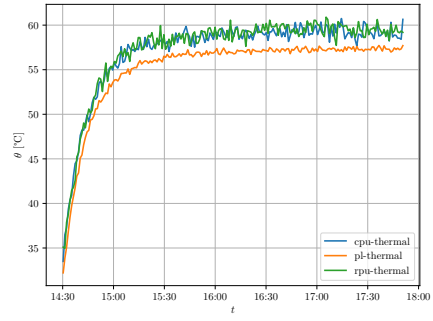


Figure 2.2: Measured System Temperature After Startup

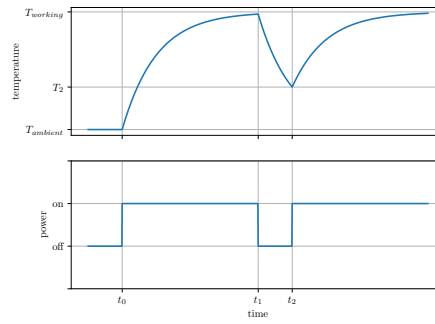


Figure 2.3: Expected System Temperature over Time for Interrupted Power

reflector peak will have a certain bandwidth, and other peaks at higher and lower frequencies will be present due to incomplete shielding and/or unwanted reflections. Also, the reflector peak may wander if the setup geometry moves. For analysis, system runtime and temperature cannot be considered independent variables, as illustrated in figure 2.3: The system starts at ambient temperature, heating up and approaching a stable operating temperature on turning on ( $t_0$ ), and cooling back down after turning off ( $t_1$ ).

### 2.1.2 Results

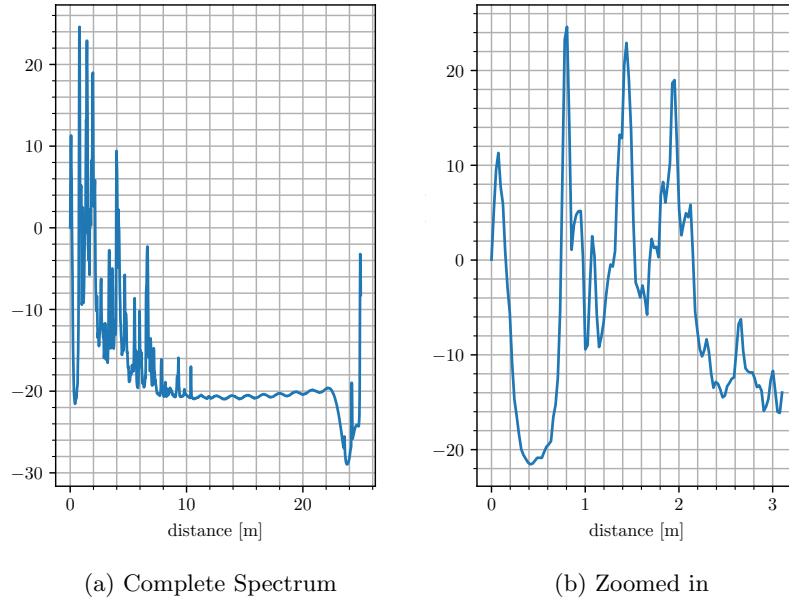


Figure 2.4: Mean Intensity Spectrum

#### Preprocessing and Analysis

Because of the aforementioned imperfections in the experiment, some preprocessing is required to analyze the systematic offsets present in the radar signal. Multiple additional peaks in the spectrum are visible in figure 2.4; indeed, the maximum peak is not even caused by the reflector. It is therefore necessary to limit the analysis to only the FFT-bin at the maximum of the peak caused by the reflector.

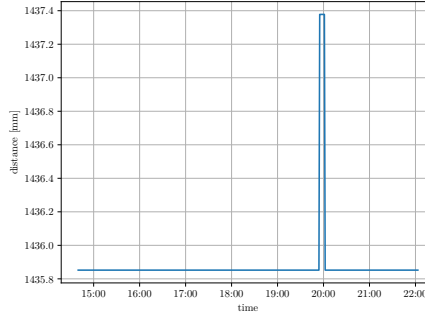


Figure 2.5: Change in reflector distance as measured by iMCR

The measurement environment also exhibits some minor changes in temperature and humidity, which can result in the geometry to shift by a few millimeters. This shows by the spectral maximum shifting over time, as seen in figure 2.5.

In the following analysis, the main metric is the complex ratio of the maximum FFT-bin to its initial value. Using a logarithmic representation of this ratio, it can be represented as a level difference [dB] and a phase difference [°].

### Effects of System Temperature and Runtime

Multiple measurements have indicated that, while the amplitude rarely varies by more than 1 dB, the phase is not as stable over time. Typically, the mean phase drifts by up to  $50^\circ$  in the hours after system startup, with the rate of change reducing after around four hours. However, it has to be noted that there is no clear correlation between phase drift and temperature: the phase continues to drift after the system temperature stabilizes; the reduction in drift only occurs hours after the system has reached a stable temperature of approximately  $60^\circ\text{C}$ .

### Effects of Self-Calibration

As described in the specification, the AWR2243P-chips undergo a self-calibration upon initialization. This initialization can be triggered by either restarting the entire system or by re-writing the configuration registers on the radar chips. Indeed, this initial calibration can be observed in the data (cf. 2.7). After the connection with the radar has been re-established, the following effects are visible:

- slightly increased level: the level in each channel increases by approximately 0.3 dB
- increased incoherence: after re-starting the system, the drift in both level and phase is distributed more broadly
- mean phase: the mean phase drift changes by up to  $5^\circ$

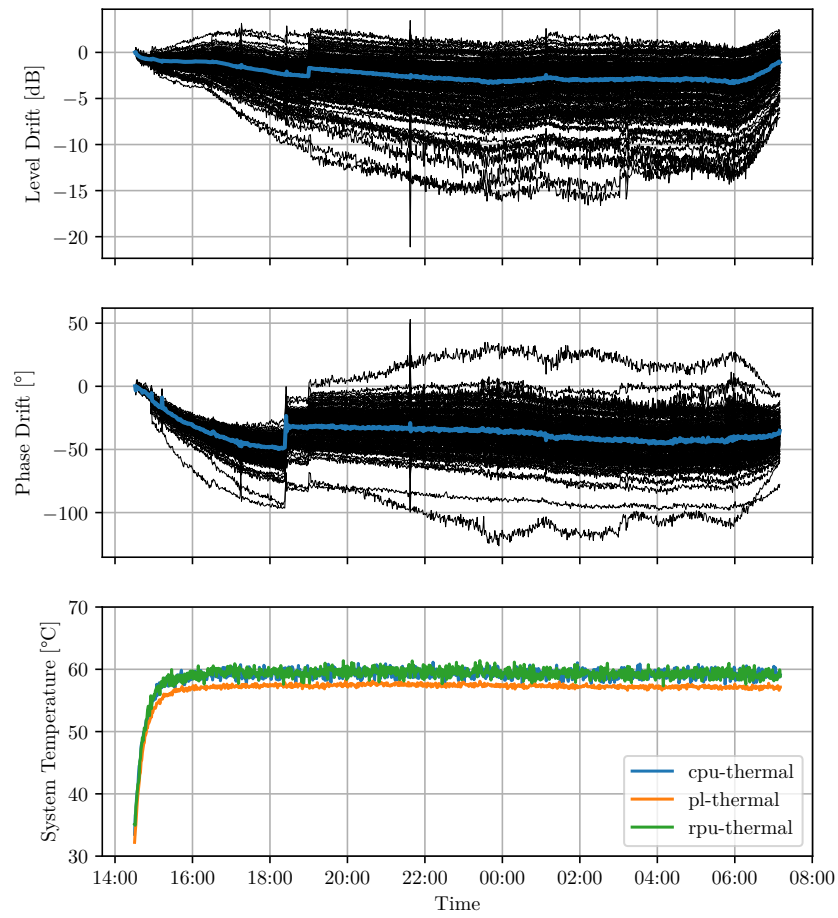


Figure 2.6: Recorded drift over night

### Differences between Antenna Pairs

Comparing the amplitude recorded by all antenna pairs, no channel in particular stands out. When looking at the different channels phase drifts, it can be seen that the array becomes less coherent over time. The distribution of phase shift across channels seems roughly gaussian, with increasing variance over time. No antenna pair seems more prone to incoherence than the rest: across measurements, the maximum outlier (in terms of divergence from the mean phase) cannot be associated with a chip or antenna.

### Effects of the Recorded Frequency and Angle

- ?

### Conclusion

The systematic offsets of the system are now better described. While the amplitude of the measured signal is relatively stable, the phase is affected more strongly. All channels' phases drift from both their initial value and each other over time. It can also be demonstrated that restarting the radar frontend has an effect on the phase, since the frontend undergoes an automatic calibration each time. No clear bias within the array has been found, seeing that across multiple measurements, all channels seem to be affected similarly.

Overall, it has been demonstrated that the radar system cannot be considered ideal and its imaging fidelity will be affected by the growing incoherence during long runtimes. Furthermore, restarting the system will change the systematic offsets due to the automatic calibration of the radar frontend hardware. Adaptive online calibration would be required to deal with these effects.

To limit the scope of this thesis, the focus is set on the offline-part of the calibration process. Since the speed at which the array incoherence grows is limited, it can be considered static during sufficiently short measurements. Also, because these offsets are affected by the automatic calibration of the system, the calibration has to be repeated on every startup.

## 2.2 Calibration

In this section, the array's antenna gains are measured and then analyzed. The measured antenna gains can then directly be employed as weights for the back-projection algorithm, resulting in a calibrated array.

### 2.2.1 Setup

To measure the antenna gains locationally, the sensor is mounted on a vertical rotating axis. Rotating the axis allows a corner reflector to be observed from

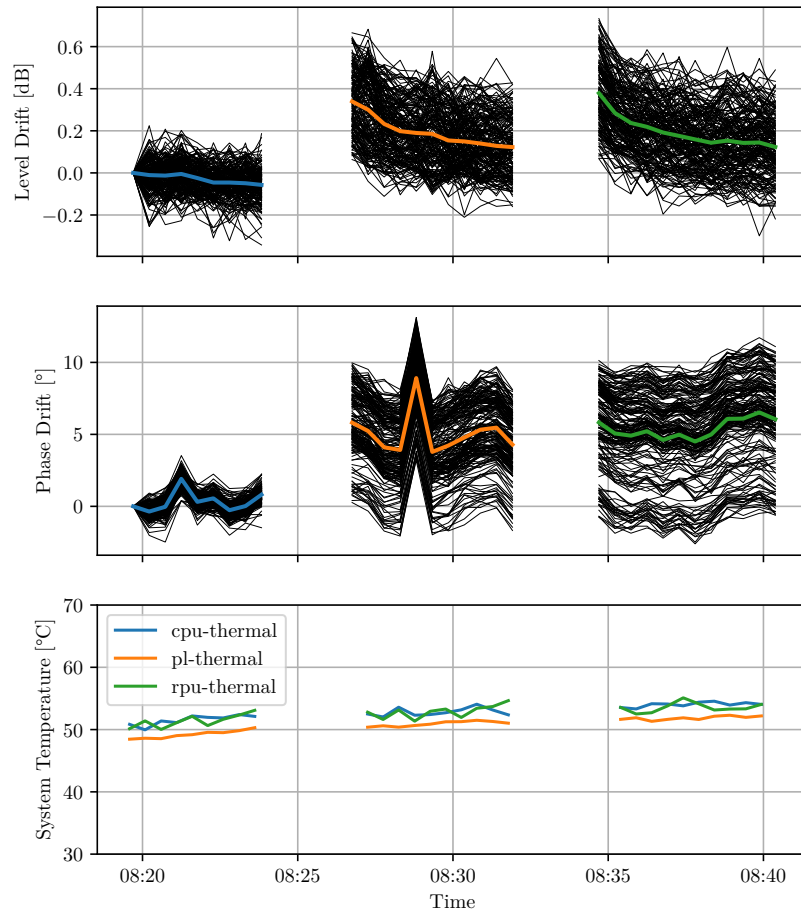


Figure 2.7: Recorded drift and temperature with system restart

multiple angles, while retaining a fixed distance. Doing this measures the antenna gain in azimuth; to measure the antenna gain in elevation, the sensor is mounted on the same axis to rotate around its horizontal axis. These two measurements are repeated for multiple reflector distances.

While the relative position of the rotating axis can be recorded with a decent resolution of around  $0.01^\circ$ , the absolute positioning of the reflector is hard to achieve with the same accuracy. The sensor itself can however be used to improve positioning: during setup, the phase of the peak caused by the reflector is displayed. Minimizing the phase differences between the array's channels ensures that the reflector be located at boresight. These measurements are repeated with multiple distances of the reflector.

The measurements are conducted outdoors to make room for longer distance measurements. This however means that the recorded scene is not free of interference.

Several trees and bushes are located at the edge of the scene. Extra interference and reflections are caused by the floor. It is also not perfectly level, varying in height by up to 1 m, which means that the reflector is not always exactly at the same height. The sensor mount also causes some problems: when the sensor is mounted on its inside, the rotational axis passes exactly through the antenna plane, but some shading is occurs when the reflector is on the same side as the sensor mount's diagonal reinforcement. When the sensor is mounted on the outside, the rotational axis is no longer in the antenna plane, adding complexity and inaccuracy to the subsequent analysis.

## 2.2.2 Results

### Preprocessing and Analysis

The expected behavior is formulated in the signal model (see equation 1.8ff.):

$$y_k(t = mT_s) = G_k(\vec{r})e^{-j\omega\tau_k mT_s}, \quad (2.2)$$

$$\text{where } G_k(\vec{r}) = \frac{A_k A_S(\theta_S, \phi_S)}{R_k^2} e^{-j\omega_0 \tau_k + \varphi_k} \quad (2.3)$$

$$\text{and } A_k := A_{Tx,i} \cdot A_{Rx,j} \text{ for } k = N_{Tx}i + j \quad (2.4)$$

A constant channel gain  $A_k$ , resulting from the transmitting and receiving antenna gains, is attenuated with increasing distance, with  $|G_k| \propto \frac{1}{R_k^2}$ . The effect of the angle of arrival on the gain is represented by the factor  $A_S(\theta_S, \phi_S)$ , which is normalized such that  $A_S(\theta_S, \phi_S) \in [0, 1]$ . A constant channel phase offset  $\varphi_k$  is set back proportionally to the time of flight  $\tau_k = 2R_k/c$ .

The goal of the subsequent analysis is twofold: to extract all parameters of the above signal model while identifying and removing interference through processing.

Limiting the analysis to a single range bin will work towards both reducing interference and extracting parameters: ideally, the DFT spectrum of the IF signal consists of just a single peak, weighted with the locational gain  $G_k(\vec{r})$  (see eqn. 1.14). Thus, the parameters of the locational gain can be extracted if the correct bin  $\hat{\Omega}$  is picked:

$$\hat{\Omega} = \dot{\omega} \tau_k(\vec{r}_S) T_s \quad (2.5)$$

$$= \dot{\omega} \frac{2R_k}{c} T_s \quad (2.6)$$

$$\Rightarrow \mathcal{F}_m\{y_k[m]\}(\Omega = \hat{\Omega}) = G_k(\vec{r}_S) \quad (2.7)$$

The relation between a range bin  $\Omega$  and its corresponding range  $r$  is

$$\Omega = r \cdot \frac{4N_{fft}\dot{\omega}}{c_0 f_s} \quad (2.8)$$

### Range Estimation

In order to improve the accuracy of the subsequent analysis, the exact position of the reflector is estimated from the radar data. To do this, numerical optimization is employed to find the parameter set  $\hat{R}_s, \hat{\theta}_s, \hat{\epsilon}$  that minimizes the difference between a range estimate  $\hat{R}_{k,l}$  and the range spectral peak  $R_{k,l}$  for all channels  $k$  and recorded orientations  $l$ :

$$R_{k,l} = \arg \max_r \mathcal{F}_m\{y_{k,l}[m]\} \left( \Omega = \frac{N_{fft}r}{R_{max}} \right) \quad (2.9)$$

The range estimate  $\hat{R}_{k,l}$  is determined geometrically from the distances of each channel's transmit and receive antenna to the reflector. If the sensor is mounted to rotate in azimuth, the range depends on the rotation angle  $\theta_l$ :

$$\hat{R}_{k,l} = \frac{\|\vec{r}_{TX,k} - \vec{r}_S(l)\| + \|\vec{r}_{RX,k} - \vec{r}_S(l)\|}{2} \quad (2.10)$$

$$\vec{r}_{TX,k} = \begin{bmatrix} x_{TX,k} \\ y_{TX,k} \\ \hat{\epsilon} \end{bmatrix}, \vec{r}_{RX,k} = \begin{bmatrix} x_{RX,k} \\ y_{RX,k} \\ \hat{\epsilon} \end{bmatrix}, \quad (2.11)$$

$$\vec{r}_S(l) = \begin{bmatrix} (\hat{R}_S - \hat{\epsilon})\sin(\hat{\theta}_S - \theta_l) \\ 0 \\ (\hat{R}_S - \hat{\epsilon})\cos(\hat{\theta}_S - \theta_l) \end{bmatrix}, \quad (2.12)$$

If it is mounted to rotate in its elevation, the reflector appears to move depending on the rotation in elevation  $\phi$ . For a given rotation angle  $\phi_l$ , it is located at

$$\vec{r}_S(l) = \begin{bmatrix} 0 \\ (\hat{R}_S - \hat{\epsilon})\sin(\hat{\phi}_S - \phi_l) \\ (\hat{R}_S - \hat{\epsilon})\cos(\hat{\phi}_S - \phi_l) \end{bmatrix}, \quad (2.13)$$



In our setup, a signal is recorded with  $\theta$  (or  $\phi$ , respectively) from  $0^\circ$  to  $180^\circ$ , with the reflector located at roughly  $R_S = \{2, 8, 18, 32\}$  m and either  $\theta_S = 90^\circ$  or  $\phi_S = 90^\circ$ .

With this, the loss  $\mathcal{L}$  can be defined as the mean square difference between  $\hat{R}$  and  $R_p$ , the mean being computed as the average over all  $K$  channels and  $L$  sensor rotations:

$$\mathcal{L}(\hat{R}_s, \hat{\theta}_s, \hat{\epsilon}) = \frac{1}{KL} \sum_{l=0}^{L-1} \sum_{k=0}^{K-1} (R_{k,l} - \hat{R}_{k,l}(\hat{R}_s, \hat{\theta}_s, \hat{\epsilon}))^2 \quad (2.14)$$

Figure 2.8 shows the result of 100 iterations at an adaption rate of 0.05 at the example of three different channels, comparing the measured spectral peaks (shown as points) to the estimated position (dotted line) of the reflector. Only a subset of orientations is used for the estimate, namely  $-50^\circ < \theta_l - 90^\circ < 20^\circ$ .

For the first three measurements, the peak location oscillates around the estimate by 1 to 2 cm. The root mean square error is reduced to 11 mm. The fourth measurement has higher noise, with no clear line being visible in the spectral peaks.

### Amplitude

First, the recorded amplitudes are analyzed, beginning with the influence of the angle of arrival. To do this, each channel's range FFT spectrum's amplitude is evaluated at the respective calculated peak location  $\hat{\Omega}$ , and then normalized by dividing it by its maximum.

The first parameters to extract are the three factors  $A_{Tx}$ ,  $A_{Rx}$  and  $A_S(\theta_S, \phi_S)$ . Since the angle of arrival's impact has been constrained to  $[0, 1]$ , we know that

$$\max_{\theta, \phi} |G_k(R, \theta, \phi)| = \frac{A_k}{R^2} \quad (2.15)$$

With that, an estimate of the channel gain  $A_k$  at exactly 1 m can be obtained via linear regression. An example linear regression is shown in figure 2.9, and the resulting estimates with their standard deviations are summarized in figure 2.10.

To now separate the estimated channel gains  $\hat{A}_k$  into individual antenna gains  $\hat{A}_{Tx,i}$  and  $\hat{A}_{Rx,j}$ , receive antenna 0 is chosen as a reference, i.e.  $\hat{A}_{Rx,0} := 1$ . All measurements with receive antenna 0 are therefor used to directly measure the transmit antenna gains:

$$\hat{A}_{Tx,i} = \hat{A}_{k=N_{Tx}i} \text{ for } i = 0 \dots N_{Tx}-1 \quad (2.16)$$

With that, the least-squares estimate of the receive antenna gains becomes

$$\hat{A}_{Rx,j} = \frac{1}{N_{Tx}} \sum_{i=0}^{N_{Tx}-1} \frac{\hat{A}_{k=N_{Rx}i+j}}{\hat{A}_{k=N_{Rx}i}} \quad (2.17)$$

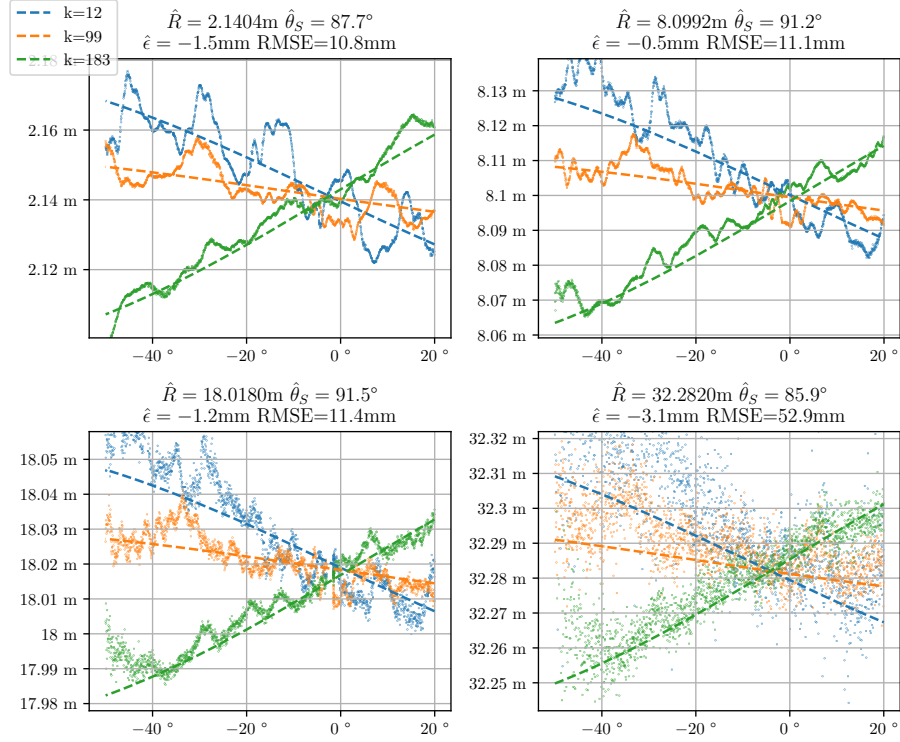


Figure 2.8: Example Optimization Results

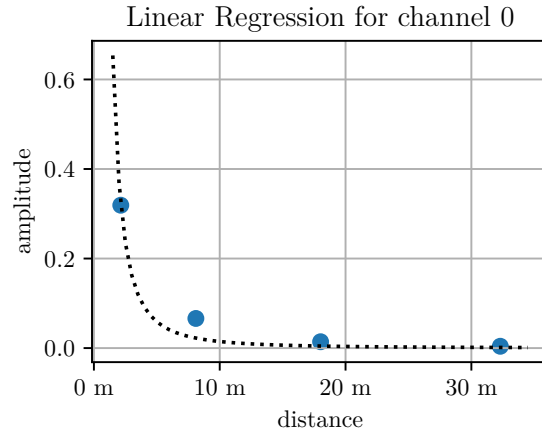


Figure 2.9: Example Channel Gain Linear Regression

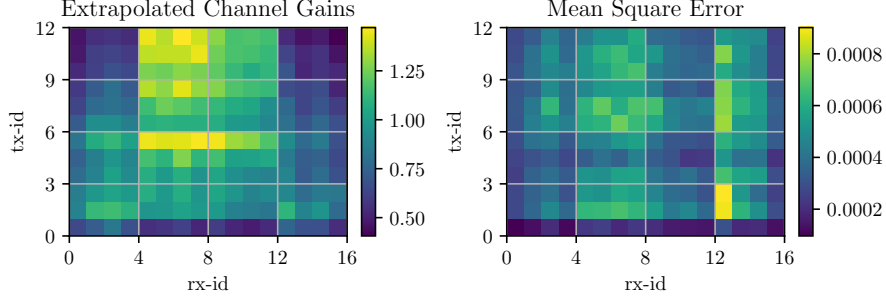


Figure 2.10: Example Channel Gain Linear Regression

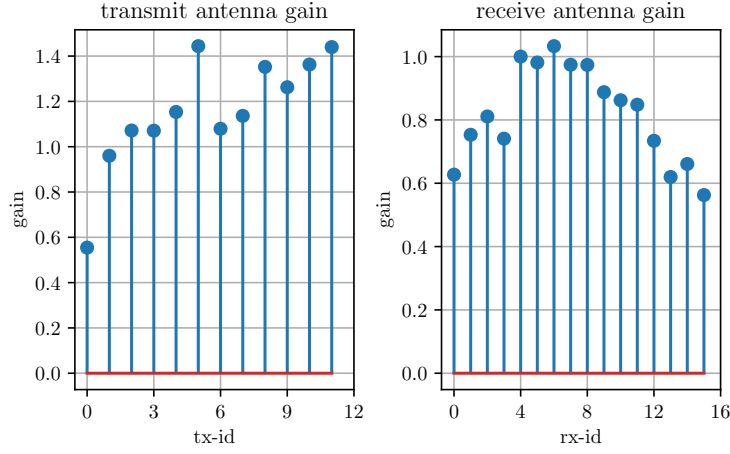


Figure 2.11: Estimated Antenna Gains

The resulting antenna gains are shown in figure 2.11. Further measurements would be required to reduce the substantial error bars. A next step would consist of a measurement setup with a linear axis moving the reflector, which would generate substantially more sample points for the linear regression.

Having estimated channel gains and outlined a method for separating them into the transmit and receive antenna gains, we can now turn to analysing the angle-of-arrival characteristics. Assuming the optimal range bin  $\hat{\Omega}$  is evaluated each time, we get

$$\left| \mathcal{F}_m \{y_k[m]\}(\Omega = \hat{\Omega}) \right| = \frac{A_k A_S(\theta_S, \phi_S)}{R_k^2} = |G_k(\vec{r}_S)| \quad (2.18)$$

Dividing that by the maximum gain (2.15) yields

$$\frac{|G_k(\vec{r}_S)|}{\max_{\theta, \phi} |G_k(R, \theta, \phi)|} = A_S(\theta, \phi) \quad (2.19)$$

Figure 2.12 provides an overview by displaying the mean channel characteristic for each measurement. It can be seen that the gain is strongest when the target is directly in boresight, tapering off when the target is off-center. The reduction in gain is stronger when the target moves off to the side in the elevation, than in azimuth. While the target remains stronger than background noise up until an azimuth angle of around  $-75^\circ$  to  $75^\circ$ , it can only be seen in an elevation angle sector from  $-25^\circ$  to  $25^\circ$ .

The graphs of the horizontal measurements appear slightly asymmetrical, an effect which is investigated in the following.

A possible explanation for the asymmetry is the sensor mount, which protrudes out on the right side of the array, attenuating the signal received by antennas on that side when the reflector is behind said protrusion.

Investigating the individual channel gains (c.f. 2.13) gives a first indication: the asymmetry is most pronounced when comparing the range of  $30^\circ$  to  $60^\circ$  to its counterpart of  $-30^\circ$  to  $-60^\circ$  for the horizontal measurements. Namely, in the former range, the gain seems to oscillate every 16 channels.

To explore further, figure 2.14 zooms in on one period. It shows the channel gain of the horizontal measurements for angles  $30^\circ$  to  $60^\circ$  of the channels in which transmit antenna 0 is active, arranged by the horizontal position of the receive antenna, from left to right. It can now be seen that the channel gain of antennas closer to the sensor mount's protrusion drops in amplitude at lower angles than that of the antennas further away from it, confirming that the sensor mount is responsible for the asymmetry. To get a more accurate estimate of the channel characteristics, the measurements have to be repeated with the sensor mounted on the outside.

With this, the individual antenna gains and the channel characteristics have been extracted from the data. In the next step, the recorded phases are analyzed.

## Phase

The first step in extracting the phase parameters from the recorded data is yet again evaluating the signal's DFT phase at the optimum range bin  $\hat{\Omega}$ , which

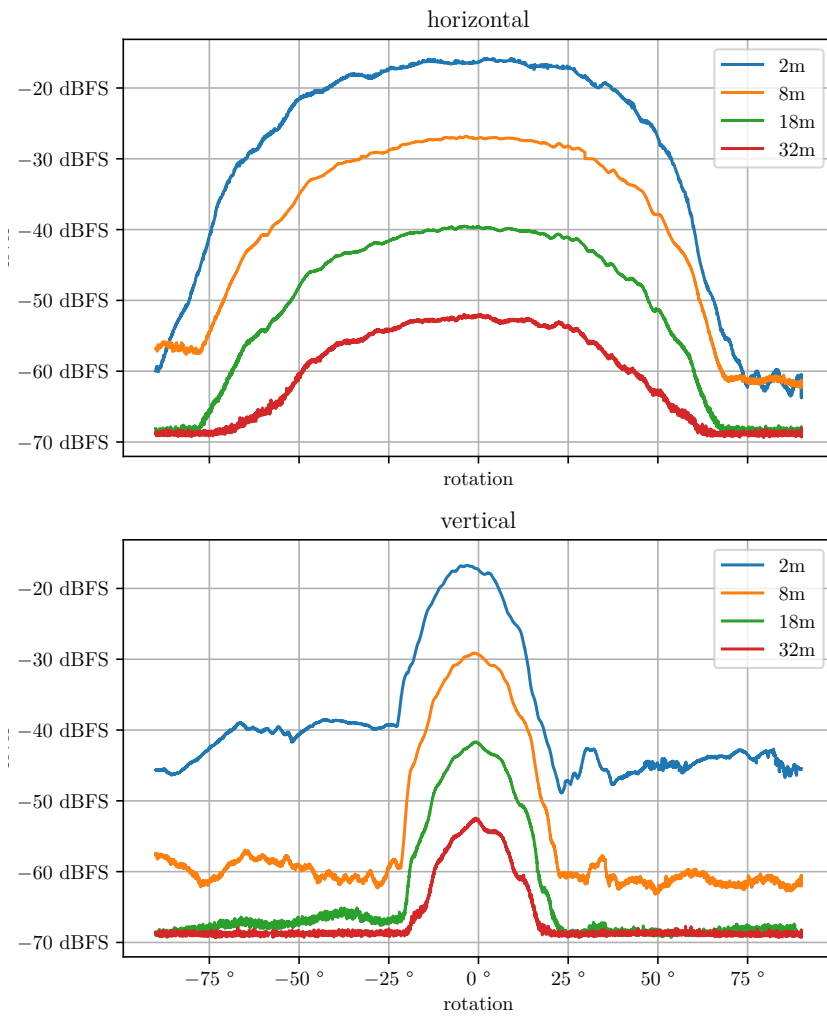


Figure 2.12: Mean Amplitude for multiple reflector distances

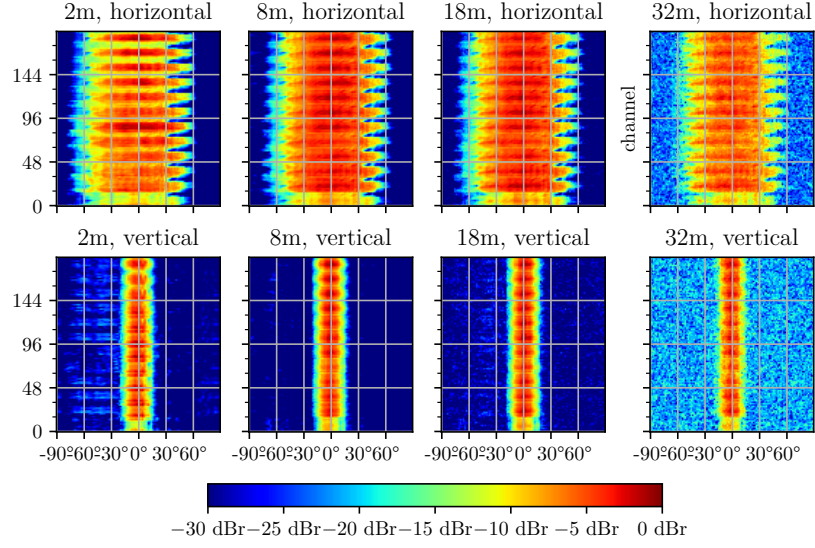


Figure 2.13: Channel-wise amplitude for multiple distances

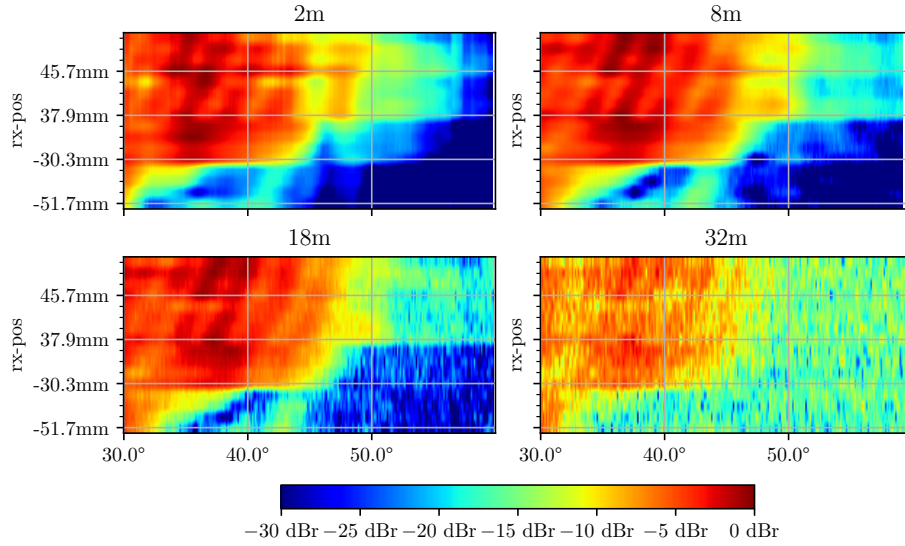


Figure 2.14: Channel-wise amplitude for multiple distances, channels arranged by Rx antenna position, only Tx antenna 0 active

according to (2.7) yields

$$\arg \mathcal{F}_m\{y_k[m]\}(\Omega = \hat{\Omega}) = \arg G_k(\vec{r}_S) \quad (2.20)$$

$$= \omega_0 \tau_k + \varphi_k \quad (2.21)$$

$$\text{with } \varphi_k = \varphi_{Tx,i} + \varphi_{Rx,j}, k = N_{rx}i + j \quad (2.22)$$

$$\text{and } \tau_k = \frac{2r_S}{c_0} \quad (2.23)$$

Ideally, the channel phase offset should be constant for every

### **Excentricity Optimiziation**

### **Antenna Separation**

### **Conclusion**

## Chapter 3

# Image Reconstruction

- recap results of last chapter - restate motivation of imaging - chapter overview

### 3.1 Implementation

- pytorch advantages: - parallel processing for tensors - API for c++ - CUDA-capabilities - pre-calculating BP weights - how to use measured gains - increased performance with ifft

### 3.2 Results

- side-lobes - compare to array gain - computational intensity ? - azimuth-range and 3D images



# List of Figures

2.1	Measurement Setup . . . . .	15
2.2	Measured System Temperature After Startup . . . . .	15
2.3	Expected System Temperature over Time for Interrupted Power . . . . .	15
2.4	Mean Intensity Spectrum . . . . .	16
2.5	Change in reflector distance as measured by iMCR . . . . .	17
2.6	Recorded drift over night . . . . .	18
2.7	Recorded drift and temperature with system restart . . . . .	20
2.8	Example Optimization Results . . . . .	24
2.9	Example Channel Gain Linear Regression . . . . .	24
2.10	Example Channel Gain Linear Regression . . . . .	25
2.11	Estimated Antenna Gains . . . . .	25
2.12	Mean Amplitude for multiple reflector distances . . . . .	27
2.13	Channel-wise amplitude for multiple distances . . . . .	28
2.14	Channel-wise amplitude for multiple distances, channels arranged by Rx antenna position, only Tx antenna 0 active . . . . .	28